

# Machine Learning-based Approach for Ex-post Assessment of Community Risk and Resilience Based on Coupled Human-Infrastructure Systems Performance

Xiangpeng Li<sup>1</sup>, Ali Mostafavi<sup>2</sup>

<sup>1</sup> Ph.D. student, UrbanResilience.AI Lab, Zachry Department of Civil and Environmental Engineering, Texas A&M University, College Station, TX, 77843; e-mail: xplli@tamu.edu

<sup>2</sup> Associate Professor, Urban Resilience.AI Lab Zachry Department of Civil and Environmental Engineering, Texas A&M University, College Station, TX, 77843; e-mail: amostafavi@civil.tamu.edu

## Abstract

While current approaches primarily focus on anticipatory or predictive resilience assessments of natural events, there is a limitation in the literature of data-driven analyses for the ex-post evaluation of community risk and resilience, particularly using features related to the performance of coupled human-infrastructure systems. To address this gap, in this study we created a machine learning-based method for the ex-post assessment of community risk and resilience and their interplay based on features related to the coupled human-infrastructure systems performance. Utilizing feature groups related to population protective actions, infrastructure/building performance features, and recovery features, we examined the risk and resilience performance of communities in the context of the 2017 Hurricane Harvey in Harris County, Texas. These features related to the coupled human-infrastructure systems performance were processed using the K-means clustering method to classify census block groups into four distinct clusters then, based on feature analysis, these clusters were labeled and designated into four quadrants of risk-resilience archetypes. Finally, we analyzed the disparities in risk-resilience status of spatial areas across different clusters as well as different income groups. The findings unveil the risk-resilience status of spatial areas shaped by their coupled human-infrastructure systems performance and their interactions. The results also inform about features that contribute to high resilience in high-risk areas. For example, the results indicate that in high-risk areas, evacuation rates contributed to a greater resilience, while in low-risk areas, preparedness contributed to greater resilience. In addition, the findings reveal disparities in the risk and resilience status of spatial areas where low-income residents reside. The outcomes of this study provide researchers and practitioners with new data-driven and machine intelligence-based methods and insights to better evaluate the risk and resilience status of communities during a disaster to inform future plans and policies.

**Keywords:** Machine learning, coupled human-infrastructure systems; Community resilience; Ex-post Resilience Assessment

## 1. Introduction

The majority of the existing work into community resilience to disasters and crises focuses on ex-ante (before-the-event) assessment of risk and resilience, with limited attention devoted to ex-post (after-the-event) assessment based on the actual performance of communities' coupled human-infrastructure systems. Ex-post community risk and resilience assessment involves examining and drawing conclusions about the extent of hazard impact and how effectively the coupled human-infrastructure systems performed in coping with the impacts, providing key insights for future resilience planning and strategy development (Molinari et al., 2014; Kameshwar et al., 2019). The current literature primarily emphasizes anticipatory, predictive, or ex-ante resilience assessments conducted before hazard events (Beguería, 2006; Wang et al., 2015; Yuan et al., 2022). Such analyses pay little attention to the resilience analysis at the post-event level, failing to capture, specify, and evaluate the actual status of community risk and resilience in an actual event context. In addition, the current approach to post-disaster assessments, as noted by Brown et al. (2008) and Mills et al. (2011), often relies heavily on survey methods, which are subject to information delays and data collection lags and suffer from major limitations in capturing the ex-post community performance. Another major limitation in the current approaches to ex-post risk and resilience assessments is their focus on their limited number of coupled human-infrastructure systems features. For example, some studies (Vamvakeridou-Lyroudia et al., 2020; Chen et al., 2016) focus primarily on hazard impacts, while other studies (Pant et al., 2018; Kasmalkar et al., 2020) primarily focus on infrastructure disruptions.

The emergence of large-scale data affords an unprecedented opportunity to use a broad range of features related to the coupled human-infrastructure systems performance in ex-post assessment of risk and resilience across different areas of communities. This data-driven method offers immediate understanding of risk-resilience archetypes, enhancing our ability to perform ex-post evaluation of community risk and resilience. This study focuses on conducting a data-driven machine learning-based ex-post assessment of community risk and resilience based on the interplay among coupled human-infrastructure systems performance features. To this end, using data from the 2017 Hurricane Harvey in Harris County, Texas, this study captures three components of coupled human-infrastructure systems performance (Figure 1). Using a K-means clustering method, we classified spatial areas (census block groups (CBGs)) based on their feature similarity. The obtained clusters are then analyzed based on their features patterns to specify archetype labels for each cluster based on their risk and resilience status. The clusters are categorized into four archetypes: high-risk/high-resilience (HH), low-risk/high-resilience (LH), high-risk/low-resilience (HL), and low-risk/low-resilience (LL), based on an in-depth analysis of the coupled human-infrastructure systems features in each cluster (Figure 1). This approach unveils the risk and resilience of areas of the community based on the coupled human-infrastructure systems performance related to protective actions, infrastructure/buildings disruptions, and population recovery. Specifically, the results reveal that different spatial areas exhibit varying levels of risk and resilience, confirming the existence of four archetypes of risk and resilience status. High-risk areas with greater evacuation rates experience faster recovery,

which yields a better resilience status. Conversely, in low-risk areas, residents demonstrating higher levels of preparedness, particularly in protective measures, exhibit better resilience status. The study also unveils that high-risk areas with higher income levels show a greater resilience status, while low-income areas exhibit lower resilience status, associating socio-demographic disparities in community risk-resilience profile. Enhancement of community resilience processes hinges on both ex-ante (anticipatory) and ex-post (observational) assessments. This study addresses an important gap related to the dearth of data-driven approaches for ex-post community risk and resilience assessment. The contributions of this study are fourfold. First, unlike previous approaches that assessed ex-post resilience based on infrastructure performance, in this study captures heterogeneous features related to the observed performance of the components of coupled human-infrastructure systems. Second, the computed features related to the performance of coupled human-infrastructure systems (i.e., protective actions, infrastructure/building impacts, and population activity recovery) are based on novel data sources, enabling a data-driven approach for ex-post rather than survey-based methods. Third, the use of a machine learning approach enables classifying risk and resilience of spatial areas based on the similarity of their coupled human-infrastructure systems performance features. Accordingly, the machine learning-based approach addresses the limitations of index-based methods that rely on subjective feature weights. Fourth, evaluation of the patterns gives insight into features that shape risk and resilience patterns, providing knowledge for informing future plans and actions. These contributions address the current limitations in methods for ex-post risk and resilience assessment and offer new methods and insights to interdisciplinary researchers and practitioners across disaster science, urban science, and emergency management for ex-post assessment of community risk and resilience through data-driven and machine intelligence-based methods.

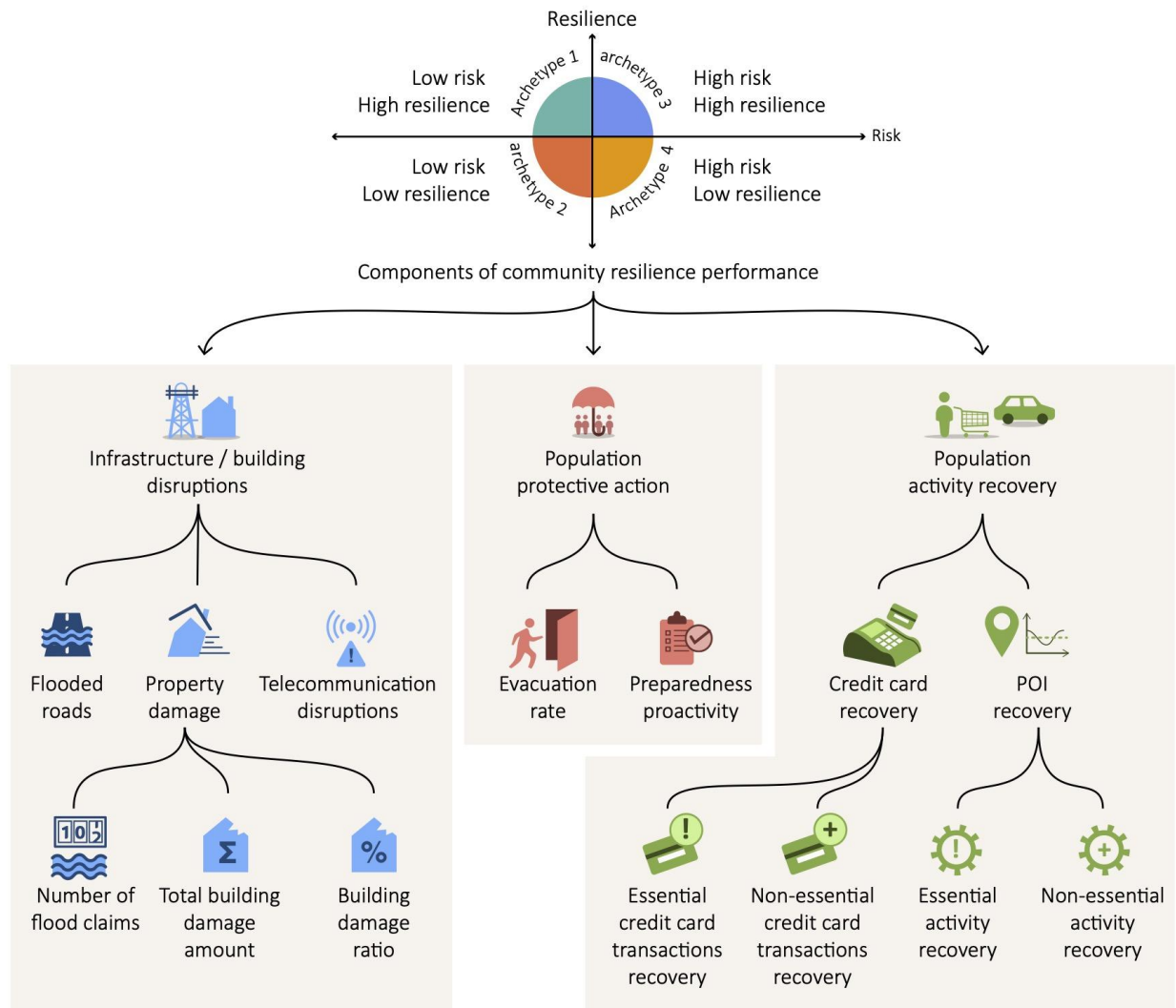


**Figure 1. Characterization of community resilience based on coupled human-infrastructure systems performance.** Coupled human-infrastructure systems performance are analyzed based various features: infrastructure/building disruptions population protective action, and population activity recovery. Each feature category has sub-components for total of 11 features. Based on the coupled human-infrastructure systems performance, spatial areas are grouped into four clusters of risk and resilience archetypes: high-risk/high-resilience (HH), low-risk/high-resilience (LH), high-risk/low-resilience (HL), and low-risk/low-resilience (LL)

## 2. Coupled human-infrastructure systems performance features

In this study, based on the existing literature, we focus on three components of the coupled human-infrastructure systems performance that shape community risk and resilience (Figure 1): population protective actions, infrastructure/building disruptions, and population activity recovery. Protective actions, particularly preparedness and evacuation, play a crucial role in

community resilience (Dong et al., 2021). Preparedness and evacuation actions moderate the extent of harm people experience and how they cope with impacts in a hazard event (Dong et al., 2019). The effectiveness of people's preparedness actions is directly linked their ability to stay shelter-in-place and cope with the impacts of hazards (Bullock et al., 2017; Lindell et al., 2006; Bronfman et al., 2019). As part of preparedness action, people would visit critical facilities to purchase items necessary items for hazard preparation, including visits to grocery stores, gas stations, and other points of interest (POIs) (Dargin et al., 2021). Accordingly, we included a preparedness feature as one of the protective action features in our study. Preparation for evacuation, with its primary objective being to minimize the risk of loss of life or injury in the case of a disaster event, is primary protective action, serves as a crucial life-saving measure, (Cova et al., 2009; Lee et al., 2022).

The second component of the coupled human-infrastructure system performance is infrastructure/building disruptions. In this study, we captured features related to road inundations, disruptions in telecommunication services, and building damage to capture infrastructure/building disruptions. The rationale for focusing on these features were the extensive disruptions to roads and buildings caused by Hurricane Harvey flooding, as well as disruptions in telecommunications services. Other infrastructure disruptions (such as power outage) were not considered since Harvey did not cause extensive power outage in Harris County. Notably, Hurricane Harvey had a profound impact on transportation, such as road inundation and accessibility, with its devastating effects lingering for weeks after the storm (Rajput et al., 2022; Coleman et al., 2020). In addition, building damage was a key factor in household displacement and dislocation during Harvey (Rosenheim et al., 2021). Hurricane Harvey also caused disruptions in telecommunication services. Spatial analyses indicate that hazards can cause internet disruptions even in unaffected areas, highlighting the complex relationship between hazard severity and internet service continuity (Gupta et al., 2023).

The third component of the coupled human-infrastructure system performance was population activity recovery. The speed at which affected populations resume their normal life activities has been shown in prior studies to provide an important indicator for community recovery (Jiang et al., 2022). Population activities are considered to recover when people settle into a pre-disaster lifestyle after coping with impacts, disrupted infrastructure is restored, and businesses resume operations. For capturing population activity recovery features, we compared variations in visits to points of interest after the hazard event and with those normal period trends against which we measured duration and speed of recovery. Prior research (Podesta et al., 2021) has shown the effectiveness of evaluating fluctuations in visits to POIs for measuring and quantifying population activity recovery.

The components of the coupled human-infrastructure systems performance discussed above were captured using features computed from various datasets. Community-scale big datasets allow us to observe the dynamics of coupled human-infrastructure systems in the risk and resilience index of communities after hazard events. Harnessing community-scale big data is instrumental in the

process of enhancing predictive flood risk monitoring, quick impact assessment, and situational awareness (Yuan et al., 2022, Praharaj et al., 2021). Multiple aspects of coupled human-infrastructure systems performance can be captured from community-scale big data and used to evaluate community risk and resilience status after the fact. In the following sections, we describe the datasets and methods used to determine the above-mentioned features.

### **3. Study Context and Datasets**

#### **3.1 Study Context**

Beginning as a tropical storm in early August 2017, Hurricane Harvey rapidly escalated to a Category 4 hurricane. By August 23, it had intensified, necessitating mandatory evacuations in several Texas counties as forecasts predict the storm as to escalate into a major hurricane (Mirbabaie et al., 2020). Making landfall about 50 kilometers (about 30 miles) northeast of Corpus Christi, Texas, on August 26. Harvey then moved towards Houston, causing severe and widespread flooding in southeastern Texas, with particularly devastating impacts occurring on August 27. These conditions persisted until August 30, 2017, and Harvey was officially declared over on August 31, leading to widespread recovery and reconstruction efforts across numerous Texas and Louisiana counties (Sternitzky DiNapoli, 2017).

From August 25 through 30, 2017, Hurricane Harvey drenched Harris County with more than 130 centimeters (50 inches) of rain, causing unprecedented flooding across vast areas of the city (Emanuel, 2017). Even though the hurricane's center bypassed Houston to the south, it brought significant rains and floods to the area, particularly in the northeast, due to a stationary front around the storm (Scientific Investigations Report, 2018). Harris County, encompassing the densely populated Houston area, experienced more than 100 centimeters (40 inches) of rain, resulting in considerable flooding and damage (Qin et al., 2020; US Census Bureau, 2022). Harvey's ferocious winds, peaking at 150 miles per hour, caused localized damage and necessitated emergency actions to avert dam failures, further aggravating the flooding and infrastructure destruction (Blake & Zelinsky, 2018; Kiaghadi & Rifai, 2019). The significance of impacts, as well as the breadth of geographic area that was impacted makes this study context a suitable setting for ex-post assessment of community risk and resilience in this study.

#### **3.2 Datasets for Features Calculation**

The data sources utilized in this study are summarized in Table 1. Our analysis focused on computing the coupled human-infrastructure systems features at the CBG level. As shown in Table 1, the components of the coupled human-infrastructure systems performance we examined include three main feature groups: population protective action, infrastructure/building disruptions and population activity recovery. Population protective action, encompassing preparedness proactivity and evacuation rate, are calculated based on location-based data. Infrastructure/building disruptions include flooded roads, property damage, and telecommunications disruptions. Population activity recovery durations were computed based on location-based data (POI data)

and credit card transactions. In total, the analysis examined 11 features related to the coupled human-infrastructure systems performance: flooded roads, number of flood claims, total building damage amount, building damage ratio, telecommunication disruptions, preparedness proactivity, evacuation rate, essential activity recovery, non-essential activity recovery, essential credit card transaction recovery, and non-essential credit card transaction recovery. There one socio-demographic characteristic feature is used to analyze the research result. A detailed description of each feature and the datasets and methods used in computing the features are presented below.

**Table 1.** Summary of coupled human-infrastructure features and datasets used for feature calculation

Feature Group	Feature	Data Description	Data Sources
Socio-demographic characteristic	Median income	Household median income in 2017	U.S. Census Bureau table data
Protective action features	Preparedness proactivity	Maximum POI visits during preparedness period relative to normal baseline in pharmacy	Safegraph, Inc; Spectus; Microsoft building footprint
		Maximum POI visits during preparedness period relative to normal baseline in gas station	Safegraph, Inc; Spectus; Microsoft building footprint
	Evacuation rate	Maximum evacuation rate from August 1 to September 31 relative to normal baseline at CBG level	Spectus
Infrastructure and building disruptions	Flooded roads	Total distance that has null traffic speed	INRIX
	Number of flood claims	The total count of flood claims within each census block group area	Federal Emergency Management Agency National Flood Insurance Program
	Total building damage amount	The actual cash value of the damage that the main property sustained is shown in terms of whole dollars.	Federal Emergency Management Agency National Flood Insurance Program
	Building Damage Ratio	The building damage ratio was determined by dividing the total number of claims by the total number of buildings in a given area.	Federal Emergency Management Agency National Flood Insurance Program, and Microsoft Building Footprints

	Telecommunicati on data	Maximum download kbps changing rate during hazard relative to normal baseline	Ookla
Recovery features	Essential activity recovery	Essential human mobility recovery data (essential POI)	Spectus
	Non-essential Activity Recovery	Non-essential human mobility recovery data (non-essential POI)	Spectus
	Essential credit card transaction recovery	Essential credit card activity	Safegraph
	Non-essential credit card transaction recovery	Non-essential credit card transactions recovery	Safegraph

- *Preparedness proactivity*

We employed the method of preparedness proactivity from Li and Mostafavi (2022) to capture the earliest maximum POI change percentage (Equation 1) at CBG level using location-based data from Spectus. Spectus acquires its data through partnerships with smartphone applications, collecting information from devices where users have consented to the collection of their location data. Mobile phone data offer detailed insights into human movement patterns on a large scale at an unprecedented spatio-temporal granularity and scale (Yabe et al., 2022). By collaborating with app developers, Spectus harnesses a variety of signals, including Bluetooth, GPS, Wi-Fi, and IoT, to compile a high-resolution geo-behavioral dataset. In our study, the preparedness period was from August 20 through August 25, 2017. To assess preparedness proactivity, we identified the peak visitation percentage change date for each CBG relative to the baseline and then determined the interval between this peak and the hurricane's landfall. Greater preparedness proactivity means people in the community prepare earlier for the natural hazard. Zero proactivity indicates people reach maximum POI change percentage on the day of the hurricane landfall. To determine the changes in POI visits due to hurricane preparations, we established baselines using POI visitation patterns related to the first two weeks in August. This period's visitation numbers capture the residents' normal POI visits with no disturbances. The preparedness rate is calculated based on visitations to pharmacies and gas stations, determined using datasets of POIs visits. Equation 1 describes the percent change of the POI visits in calculating the preparedness index of each CBG:

$$PC_{i,d,t} = \frac{V_{i,d,t} - B_{i,d,t}}{B_{i,d,t}} \quad (\text{Eq.1})$$

where,  $PC_{i,d,t}$  is the percentage change of visits to one category of POI (t) from home CBG (i) in



date (d),  $V_{i,d,t}$  is the number of visits to one category of POI (t) from home CBG (i) on date (d).  $B_{i,d,t}$  is the calculated baseline value corresponding to the date. The maximum POI visitation change percentage of certain POI is computed, and the date is recorded. The preparedness proactivity is calculated based on the difference in days between the recorded date and August 25, 2017. For example, if an area reached its maximum POI visitation change percentage on August 24, 2017, its preparedness proactivity is one day. After compiling all preparedness proactivity measures related to gas stations and pharmacies, we determine their mean value as the overall preparedness proactivity for a CBG.

- *Evacuation Rate*

For each CBG, we calculated the maximum evacuation rate by comparing evacuation rate just before, during, and after Hurricane Harvey (August 6 through September 30, 2017) with a pre-event baseline period (July 9, through August 5, 2017). We then chose the maximum percentage change for each CBG as our feature value, following the methodology of Lee et al. (2022), and using location-based data from Spectus. Only users with a minimum of 240 minutes of daily location information were included to ensure data accuracy and minimize bias. Individuals who left their home CBGs and CBGs and stayed in another CBG for at least 24 hours during Hurricane Harvey were considered to have evacuated. Here Equation 2 describes the percent change of the evacuation rate (ER):

$$\text{ER Change \%} = \frac{ER_t - ER_B}{ER_B} \quad (\text{Eq. 2})$$

$ER_t$  represents the evacuation rate on day t, and  $ER_B$  is the baseline. The maximum evacuation rate change percentage is the feature for evacuation in this study.

- *Flooded Roads*

Flooded road networks limit access to emergency services (Yuan et al., 2022; Dong et al., 2020; Bhavathrathan & Patil, 2015). Harris County road segment traffic data from August 20 through September 11, 2017, obtained from INRIX, provided average traffic speeds for each road segment at 5-minute intervals, along with historical average speeds for comparison. Following the approach of Fan et al. (2020) and Yuan et al. (2021b, 2021c), road segments displaying a null value for average traffic speed were categorized as flooded during Hurricane Harvey. Using mapping tools, we created LineString representations of flooded roads to visualize their paths. By overlaying these lines with CBG boundaries, we identified where flooded roads were encompassed by a CBG polygon. We quantified the total length of flooded roads within each CBG polygon. These lengths represent the total null distance in each CBG polygon, indicating the extent of flooded roads within those areas.

- *Number of flood claims*

The insurance claim data utilized in this study was sourced from the FEMA National Flood Insurance Program (NFIP) (FEMA, 2023). FEMA manages the NFIP by overseeing the proper processing of insurance applications, determining accurate insurance premiums, and handling the renewal, modification, and cancellation of insurance policies. This data set provides details on NFIP claims transactions, and the number of claims in a given area was determined by calculating the total count of insurance claims filed by policyholders in each CBG.

- *Total building damage amount*

The total building damage amount, sourced directly from the National Flood Insurance Program, represents the actual cash value of damage incurred by the main property, expressed in whole dollars. We aggregated this data to the total building damage amount for each CBG area by summing all the reported damage amounts.

- *Building damage ratio*

The building damage ratio was determined by dividing the total number of claims by the total number of buildings in a given area. The number of claims has been mentioned before, and the data on the total number of buildings was from Microsoft Building Footprints. The Bing Maps and Microsoft Maps & Geospatial teams have extracted a comprehensive dataset consisting of 129,591,852 building footprints across the United States (*Microsoft/USBuildingFootprints*, 2018/2024).

- *Telecommunication disruptions*

Ookla data encompasses cellular internet speeds, including specific metrics like upload and download rates from mobile devices, latency, and location-based information about both the device and the server (Ookla 2023). In our research, we focus on using the download kbps changing rate as the telecommunication data from August 10 to September 8, 2017. The download kbps changing rate was assumed to be the maximum changing rate during this period. For our analysis, we leveraged data provided by Ookla, which offers comprehensive insights into internet capabilities, including cellular internet speeds. This dataset includes vital metrics such as upload and download rates from mobile devices, latency, and geolocation information about the devices and servers involved (Gupta et al., 2023).

In our specific study, in order to record the maximum telecommunication disruptions, we concentrate on the maximum changing rate of download speeds in kilobits per second (kbps) from August 10 through September 8, 2017. To establish a baseline for normal telecommunication operations, we calculated the average download speed during the first two weeks of August. This period is chosen to reflect a typical pattern of telecommunication use without the influence of an impending natural disaster. The measure of the maximum telecommunication disruption is then determined by the Equation (3).

$$\text{Maximum Download Speed Change \%} = \frac{\text{Speed}_B - \min(\text{Speed}_t)}{\text{Speed}_B} \quad (\text{Eq.3})$$

where  $\min(\text{Speed}_t)$  represents the minimum download speed on day t from August 24th and September 3rd, 2017, and  $\text{Speed}_B$  is the baseline.

- *Essential and non-essential activity recovery and credit card transaction recovery*

To create smart, resilient, and sustainable urban environments, urban planned need an understanding of how extreme weather events affect human activities (Chen et al., 2020; Zhang et al., 2022). creating. The dataset comprising points of interest visitation patterns was obtained from Spectus; the dataset related to credit card transactions was sourced from SafeGraph. In line with methodologies used in prior research (Podesta et al., 2021; Li et al., 2023; Jiang et al., 2022), this study uses essential activity recovery, non-essential activity recovery, essential credit card transaction recovery, and non-essential credit card transaction recovery. The period from August 1 through August 21, 2017, was designated as the pre-disaster phase. During this time, baseline levels for the four features were established using a seven-day moving average of daily visits to various POIs, and that level serves as a reference for comparing pre-disaster visitation patterns to POIs. This percentage change highlights the variance between daily visits to each POI category before and after the hurricane. In Equation 4, the daily value refers to the actual observed visits to POIs on a given day, while the base value acts as the reference point for the normal activity period before the disaster. The change percentage is then calculated to reflect variations in the daily visit numbers for each category, relative to the baseline, using a seven-day rolling average to smooth the data over seven-day intervals:

$$7 - \text{day Rolling}_{avg} = \sum_{d=1}^7 \frac{\text{Daily value} - \text{Base value}}{\text{Base Value}} 100\% \quad (\text{Eq. 4})$$

Resilience curves for POIs were derived by plotting seven-day rolling averages. In this study, the term duration of recovery and is defined as the time at which the seven-day rolling average of visits to POIs attains 90% of the baseline values established prior to the disruption. This calculation enabled us to determine the average time needed for each area to achieve recovery.

#### 4. Methodology

After computing the features related to the coupled human-infrastructure systems features, we implemented unsupervised machine learning to cluster CBGs based on their features. Figure 2 presents a detailed illustration of our analysis steps. The first step in our approach involved employing the K-means cluster method to organize the data into four distinct risk-resilience archetypes based on their feature values. The final step of analysis involved delineating features for each risk-resilience archetype that contributed to resilience of CBGs based on their risk levels. This analysis also included evaluating disparities in risk-resilience archetypes of CBGs with different median income levels.

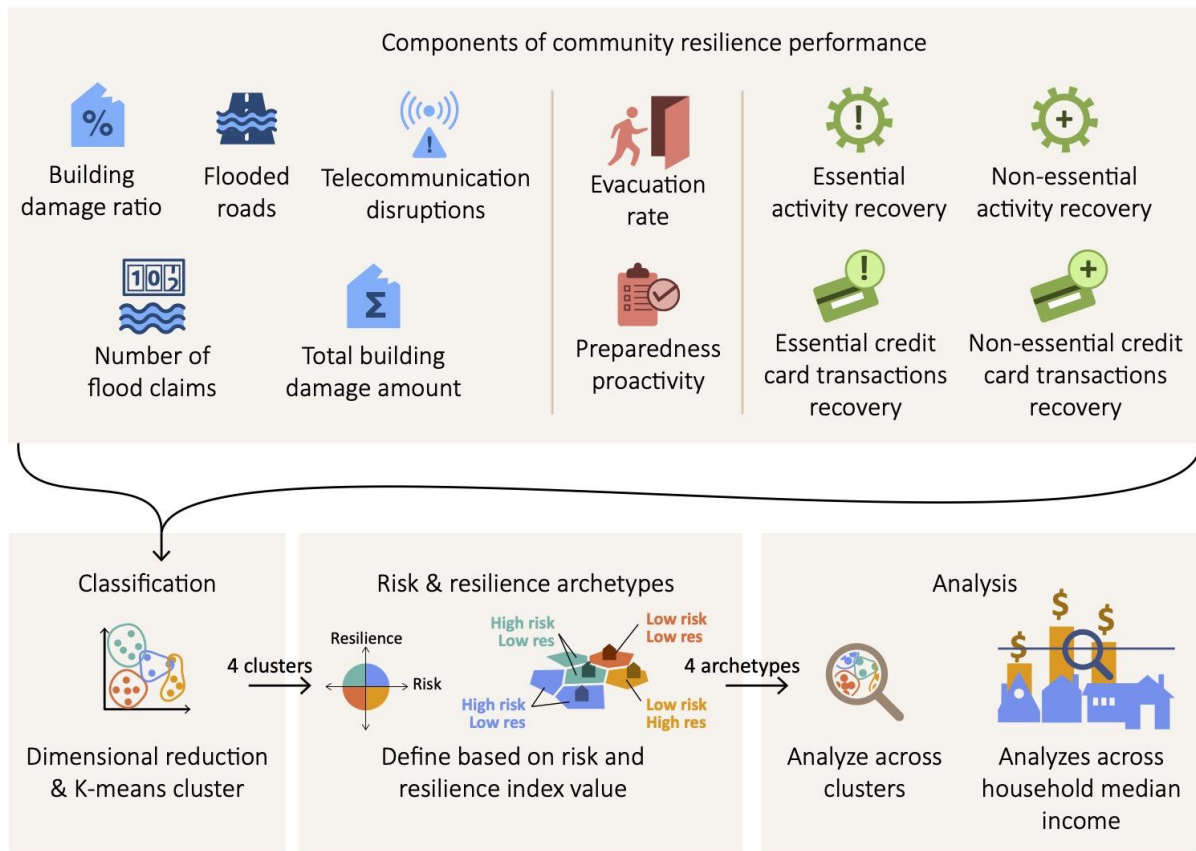


**Figure 2. The Overview of analysis steps.** Total of eleven features are classified into four clusters using the K-means algorithm. These clusters are then labeled as risk and resilience archetypes based on their feature values. Accordingly, disparities in risk-resilience archetypes of CBGs with varying median income levels are examined.

#### 4.2 Unsupervised classification based on K-means

In our research, we implemented the K-means algorithm, a method for partitioning data into distinct groups based on feature similarity. The K-means algorithm identifies centroids within the data and assigns each data point to the nearest cluster, iteratively optimizing the positions of the centroids to minimize variance within each cluster (Kodinariya, & Makwana, 2013). K-means clustering allows us to classify CBG based on their feature similarity related to their coupled human-infrastructure systems performance. Upon application of these techniques, we achieved a silhouette score of 0.5, which suggests a reasonably well-defined cluster structure (Kaufman & Rousseeuw, 1990; Hubert & Arabie, 1985; Jain & Dubes, 1988; Meilă, 2005). Figure 3 displays the four resulting clusters, each distinctively marked with a unique color.

## Clusters of Harris County, TX

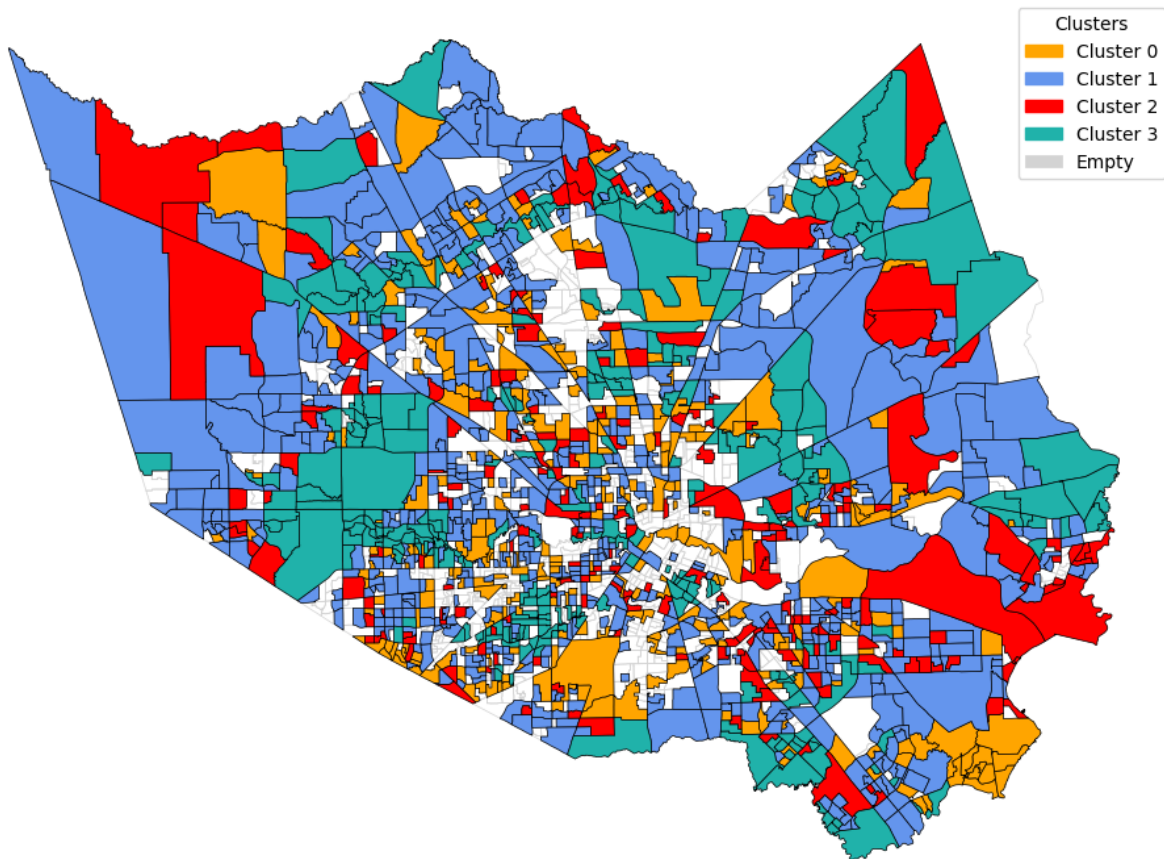


**Figure 3. Spatial Distribution of Clusters in Harris County, TX.** There are four clusters in Harris County based on the K-means clustering analysis: Cluster 0 (299 CBGs) is shaded orange, cluster 1 (662 CBGs), blue; cluster 2 (210 CBGs), red; and cluster 3 (290 CBGs), green.; and missing data, gray.

### 4.3 Risk and resilience archetypes

To assess risk and resilience status of CBGs in each cluster, we developed a risk index and a resilience index. The resilience index incorporates features related to population activity recovery—essential activity recovery, non-essential activity recovery, essential credit card transaction recovery, and non-essential credit card transaction recovery. The risk index combines the other features: flooded roads, number of flood claims, total building damage amount, building damage ratio, telecommunication disruptions, preparedness proactivity, and evacuation rate. We normalized each feature and calculated the overall median value across all features to form the composite risk and resilience index. It is important to note that the resilience index is derived as

the inverse of the overall median value of the population activity recovery features, because we considered higher resilience as indicative of a shorter recovery duration.

The scatter plot in Figure 4 displays the four clusters within the framework of risk and resilience archetypes. The median resilience value is represented by a horizontal blue dashed line, while the median risk value is indicated by a vertical green dashed line. The placement of the four clusters corresponds to their respective median resilience and risk index values. This visual analysis reveals that cluster 1 falls into the low-risk and high-resilience (LH) quadrant; cluster 0 is categorized under the low-risk and low-resilience (LL) quadrant; cluster 3 is positioned in the high-risk and high-resilience (HH) quadrant; and cluster 2 is situated in the high-risk and low-resilience (HL) quadrant. Cluster 3 exhibits the greatest level of risk yet maintains a robust resilience, suggesting an effective risk-resilience dynamic within this cluster. Conversely, cluster 0 bears the least risk but demonstrates a correspondingly low resilience, indicating a low risk-low resilience status.

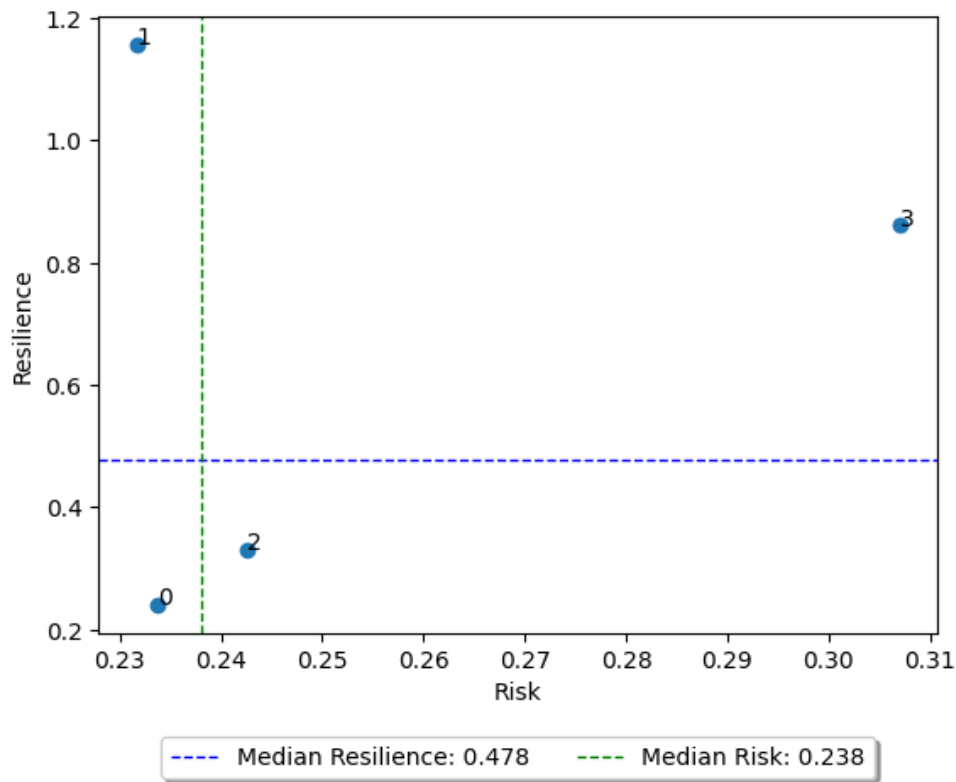


**Figure 4. Risk and resilience archetype for each cluster.** There are four resilience and risk archetypes: Cluster 1 falls into the low-risk/high-resilience (LH) quadrant; Cluster 0 is categorized under the low-risk/low-resilience (LL) quadrant; Cluster 3 is positioned in the high-risk/high-resilience (HH) quadrant; Cluster 2 is situated in the high-risk/low-resilience (HL) quadrant.

## **5. Results and discussion**

### **5.1 Spatial distribution of archetypes and their feature values**

We examined the feature values in each risk-resilience archetype. Figure 5 illustrates the spatial patterns of feature values for different risk-resilience archetypes. In the analysis, visualization of normalized feature values within their respective subplots is achieved by scaling the color mapping according to the minimum and maximum values ( $v_{min}$  and  $v_{max}$ ) observed across all clusters for each specific feature. Following this step, the median value for each cluster is calculated and used as a basis for distinguishing between clusters in the visualization. In Figure 5, the shade of light blue in the color gradient represents higher median values for a feature across clusters, with darker shades indicating lower values. The maps reveal consistent patterns in the distribution of the number of claims, the ratio of building damage, and the total amount of building damage. HH (cluster 3), in particular, shows significant levels of property damage, a trend that is mirrored in the evacuation rate pattern. The correlation between extensive property damage and higher evacuation rates in HH suggests that the severity of damage significantly influences the decision to evacuate. In addition, LL (cluster 0) is notable due to its low preparedness index, which has the lowest mean and median value. This low level of preparedness in LL could have implications for the ability of residents in these areas to cope with disaster-induced disruptions. The variations in the feature values across different clusters was further evaluated in the following section to reveal features that contributed to risk and resilience status of each cluster.

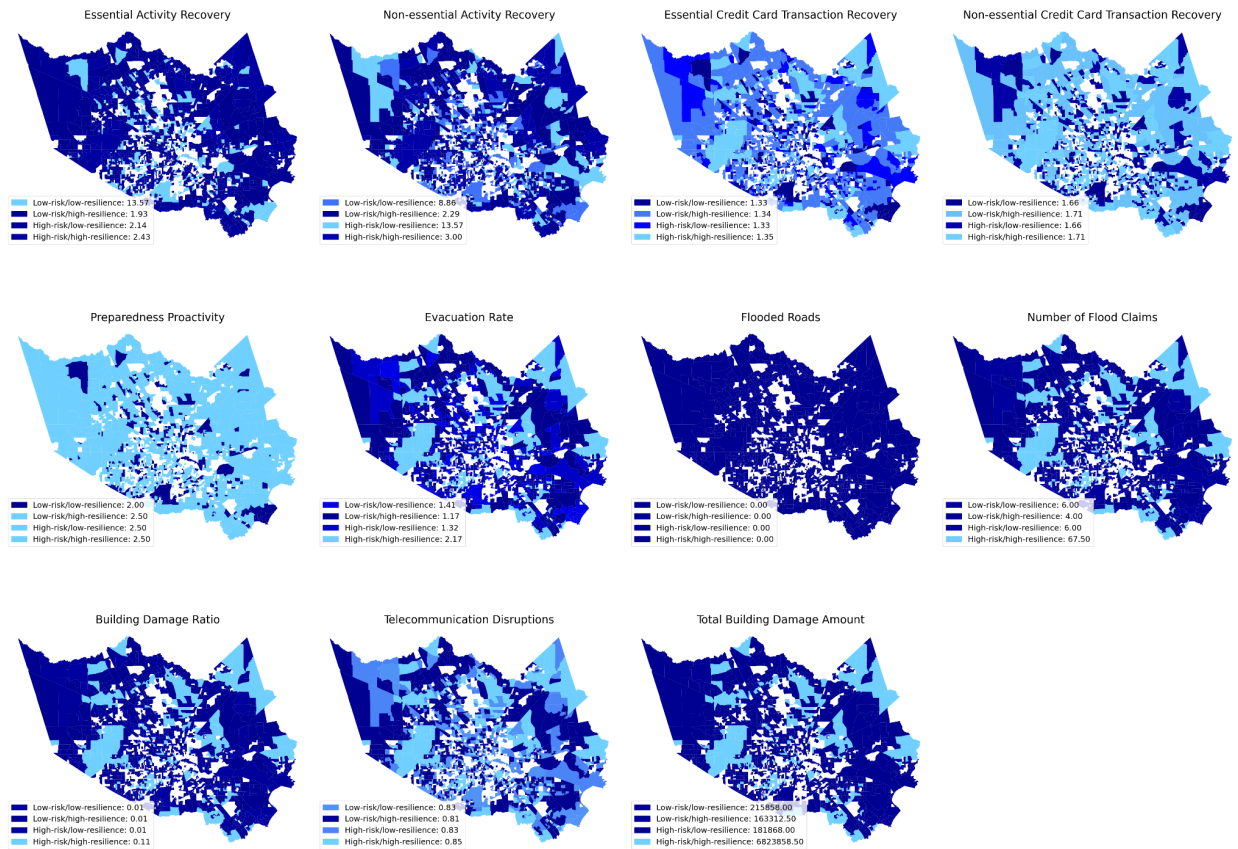


**Figure 5. The spatial distribution of four archetypes for each feature.** Lighter shades of blue signify higher median values for a feature across archetypes, while darker shades denote lower values.

## 5.2 Analysis of feature values across archetypes

Box plots depicting the range of feature values in each archetype (cluster) (Figure 6) provide a comparative analysis of features across clusters. The recovery features captured by the initial four box plots (essential activity recovery, non-essential activity recovery, essential credit card transaction recovery, and non-essential credit card transaction recovery) are components of the resilience index. The other seven box plots (preparedness proactivity, evacuation rate, flooded roads, number of flood claims, building damage ratio, telecommunication disruptions, and total building damage amount) are components of risk index. These box plots depict feature value distributions, where the boxes illustrate the interquartile range, encapsulating the middle 50% of the data, and a central line within each box marks the median value. Whiskers extending from the boxes cover the broader data range, while individual dots beyond the whiskers highlight outliers (Williamson, 1989). Solid red lines incorporated into each box denote the mean value of the respective feature for each cluster. The dashed red line across each box plot indicates the overall mean value of each feature for all clusters combined.



LL (low-risk/low-resilience) (cluster 0) shows a noticeable trend of longer recovery periods for both essential and non-essential activities, resulting in a low resilience index. This is based on the understanding that longer recovery times are indicative of lower resilience. In addition, the average values of seven other features in this archetype are predominantly lower than the collective average of LL, reinforcing its classification as a low-risk/low-resilience archetype as depicted in Figure 4. In LH (low-rise/high resilience) (cluster 1), it is observed that the average recovery times across all activities and credit card transactions fall below the general average for these features. Furthermore, the median recovery times for both essential and non-essential activities are the minimum when contrasted with other archetypes, signaling a greater resilience index for LH. The median and mean figures for evacuation rate, flooded roads, number of flood claims, building damage ratio, and total building damage amount are also the smallest relative to other archetypes, corroborating LH's classification as a group with low risk and high resilience. The mean values of non-essential activity recovery and both essential and non-essential credit card transaction recovery in HL (high-risk/low-resilience) (cluster 2) surpass the general average, indicating a lower resilience. On the other hand, HH's (high-risk/high-resilience) averages for all types of activity recovery and credit card transaction recovery fall below the overall mean, suggesting that HH (cluster 3) had a higher resilience status. Moreover, HH's mean values for the risk features exceed the overall averages, pointing to a greater risk index for CBGs in this archetype. This result aligns with the depiction in Figure 4, where HH is classified among the archetypes with both high risk and high resilience. These findings confirm the risk-resilience archetype labels designated to each archetype based on their coupled human-infrastructure systems features.

Considering that HL (high-rise/high-resilience) and HH both had high risk status, it is noteworthy to juxtapose their resilience status and difference. Notably, HH has a more substantial evacuation rate than HL, whose median evacuation rate is below the overall median. This pattern may imply either a reduced rate of evacuation in HH or economic hurdles impeding evacuation, potentially resulting in extended recovery times. On the other hand, when it comes to low-risk areas, LH demonstrates better preparedness proactivity compared to LL, whose median preparedness is below the general median. This low level of preparedness in LL highlights the importance of being well-prepared in low-risk areas to facilitate effective community recovery time. Low-risk low-resilience areas are noteworthy since they might not have experienced high risk, but they demonstrated low resilience which could be problematic if future events cause greater risks in those areas. High-risk areas with greater evacuation rates experience faster recovery, which yields a better resilience status. This result suggests that evacuation is a key factor in shaping the resilience of communities facing significant risks. Conversely, low-risk areas, areas whose residents demonstrate higher levels of preparedness, particularly in protective measures, exhibit better resilience status.

In summary, from the plots in Figure 5, we can observe that in regions classified as low-risk (LL and LH), LH exhibits a notably higher resilience status. This archetype also demonstrates a higher level of preparedness, suggesting that in low-risk areas, a well-prepared community tends to be

more resilient. In contrast, in high-risk areas (HL and HH), HH is distinguished by a more significant evacuation rate, supporting the notion that proactive evacuation enhances resilience in areas prone to high risk.

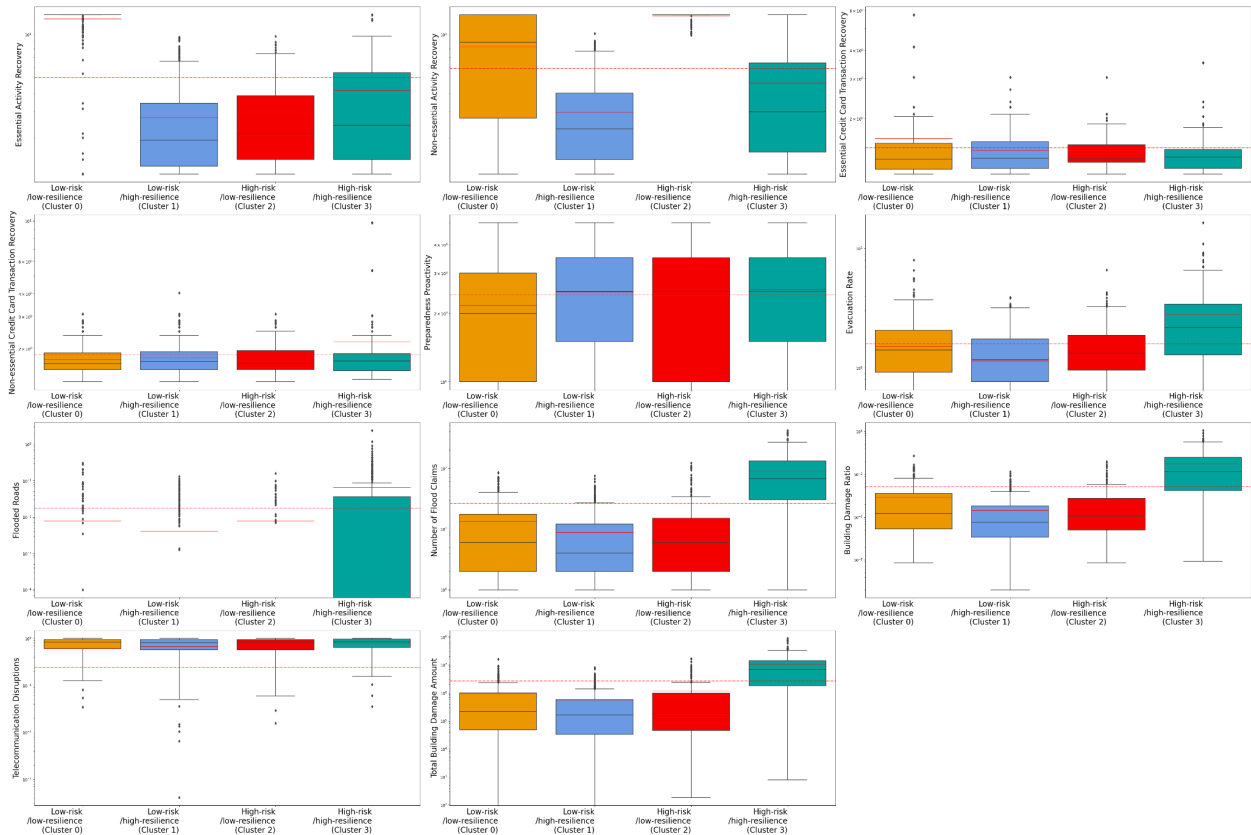


**Figure 6. Box plot of each feature across archetypes.** Each feature is represented by 11 box plots: essential activity recovery, non-essential activity recovery, essential credit card transaction recovery, non-essential credit card transaction recovery, preparedness proactivity, evacuation rate, flooded roads, number of flood claims, building damage ratio. Low-risk/low-resilience archetype is shaded orange; low-risk/high-resilience archetype, blue; high-risk/low-resilience, red; and high-risk/high-resilience, green.

### 5.3 Disparities in risk and resilience status across income groups

We examined the relationship between each archetype's household median income and their resilience status and found disparities in resilience between different income groups (Grinberger & Felsenstein, 2016; Logan et al., 2021). Figure 7 illustrates this result by presenting the median (blue bars) and mean (orange bars) incomes of residents in the CBGs of each archetype. The blue dashed line indicates the overall mean income across all archetypes; an orange dashed line represents the overall median income. Figure 8 illustrates the spatial distribution of median income of each archetype, and we can see that high-poverty neighborhoods are located directly north and

southeast of downtown. The areas east of downtown and the edges of the county generally exhibit higher income levels.

From this visual representation, it is evident that residents in CBGs in LH and HH have higher mean and median incomes compared to CBGs in LL and HL. When examining archetypes with lower resilience (HL and LL), both are characterized by incomes and evacuation rates falling below the overall median. This pattern confirms the hypothesis that limited financial resources can impede the ability to evacuate. Notably, HL, despite facing higher risk, displays a greater level of preparedness than LL, potentially contributing to its relatively higher resilience. Focusing on archetypes with higher resilience (LH and HH), both had higher median incomes and demonstrated high resilience status. This observation suggests an association between higher income levels and quicker population's activity recovery (and hence a greater resilience status). Notably, HH has higher median income than that in LL. HH, in particular, has faced the most substantial property damage and flooding, yet it also records the highest evacuation rate, emphasizing the critical role of evacuation in faster community recovery. Therefore, income emerges as a pivotal factor in bolstering resilience. HH, despite grappling with severe risks, maintains a high level of resilience, likely bolstered by its higher median income. This observation underscores the influence of economic factors in enhancing a community's capacity to recover from hazards. Conversely, limited access to resources of low-income populations impedes them from preparing and recovering from hazards (Li et al., 2023). When considering both high-risk conditions, the median income in HH is considerably greater than that in HL. This disparity may imply that financial constraints in residents of CBGs in HL could be a limiting factor in evacuation efforts. These results highlight a disparity in the risk-resilience profile of communities.

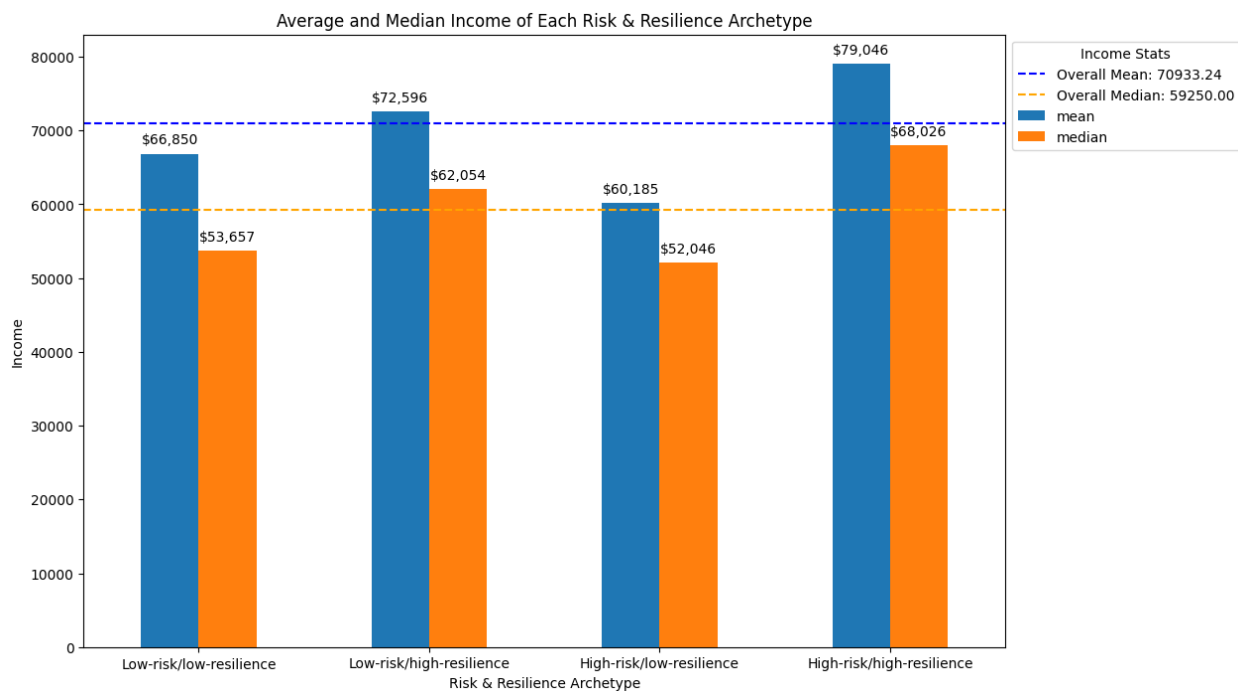


**Figure 7. Mean and median income of each archetype.** Blue bars depict median income levels; orange bars, mean income levels. The dashed blue line depicts the overall mean income across archetypes; the dashed orange line shows overall median income.

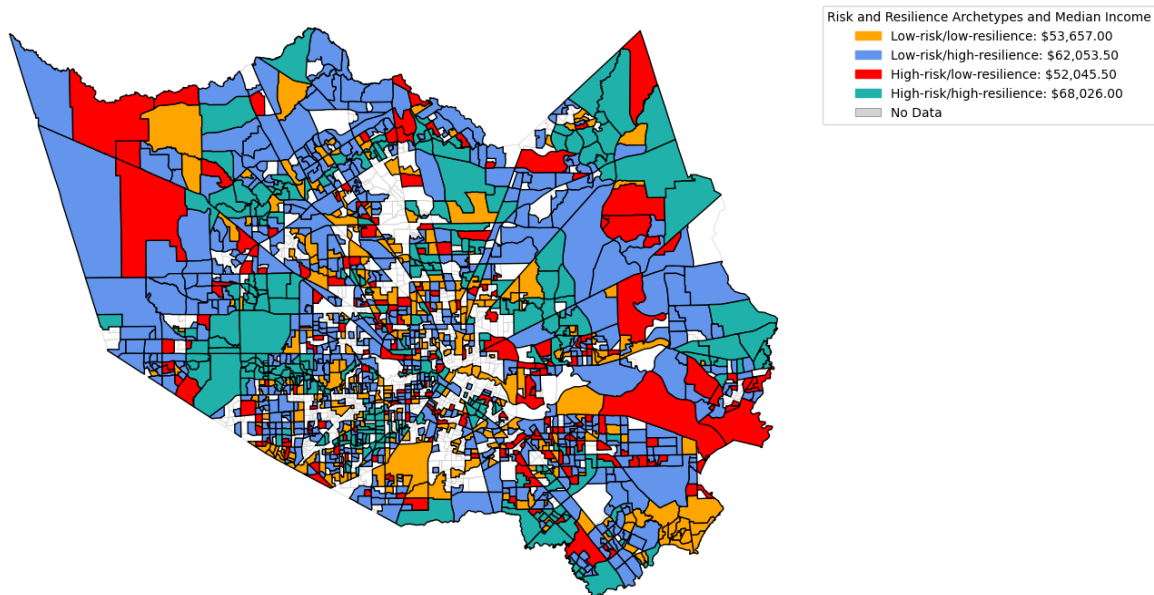


**Figure 8. Spatial distribution of median income for each archetype.** The map displays the spatial distribution of the four archetypes, each differentiated by varying median income levels. The median income of low-risk/low-resilience (cluster 0) is \$53,657.00. The median income of low-risk/high resilience (cluster 1) is \$62,053.50. The median income of high-risk/low resilience (cluster 2) is \$52,045.50. The median income of high-risk/high resilience (cluster 3) is \$68,026.00.

## 6. Concluding remarks

This study proposed a machine learning-based approach for ex-post assessment of community risk and resilience based on coupled human-infrastructure systems performance. Despite significant advancements in the interdisciplinary field of community resilience, most existing studies focus primarily on ex-ante assessments; Relatively less attention has been paid to ex-post assessments. Also, the majority of ex-post assessments are based primarily on disaster reconnaissance approaches focusing on measuring impacts and damage. Furthermore, ex-post assessments rely primarily on surveys for capturing impacts and damage, resulting in delays in data collection and assessment. Finally, the current approaches to ex-post assessment of community resilience focus mainly on single systems (e.g., transportation, housing, or businesses) and do not consider various aspects of coupled human-infrastructure performance. These limitations are addressed in this study based on evaluating various features related to coupled-human infrastructure performance computed from various data sources and by adopting a machine learning-based approach to

classify spatial areas of a community (census block groups) based on the intertwined features to unveil various risk and resilience performance archetypes.

The outcomes of this study have multiple important scientific and practical contributions. First, the study provides a novel approach to ex-post assessment of community resilience using a data-driven and machine intelligence-based approach. The method presented in this study could provide interdisciplinary researchers in the fields of disasters and community resilience with a new tool for ex-post evaluation of community resilience based on a diverse range of features related to coupled human-infrastructure systems performance. This data-driven approach could provide a more unified way for ex-post evaluation of community risk and resilience to enable comparison of coupled human-infrastructure systems performance across different events and different regions. Second, the approach presented in this study enables capturing various features related to coupled human-infrastructure performance in evaluation of community resilience. The features capture disruptions and restoration of infrastructure services, protective actions of populations, property damage, as well as life activity recovery of populations. The consideration of various features would provide a more comprehensive evaluation of community resilience compared with the existing approaches that focus primarily on performance of human or infrastructure systems separately.

Third, the features related to the coupled human-infrastructure systems performance are captured based on observational data from various sources enabling a more data-driven approach to post-disaster community resilience evaluations. Data-driven evaluation community resilience based on various coupled human-infrastructure systems performance features is essential for guiding response and recovery efforts to fairly effect resource allocation and prioritization. Fourth, the study revealed the spatial risk and resilience profile of communities based on four archetypes according to their coupled human-infrastructure systems performance. The specification of the risk-resilience archetype of communities provides essential insights for future risk reduction and resilience improvement strategies for planners and public officials. For example, in high risk and low resilience areas, future plans should aim for infrastructure systems performance while also bolstering the performance of human systems through strategies such as more effective evacuation planning and implementation. Depending on the risk-resilience archetype, resilience strategies vary. For example, evacuation should be targeted mainly for high-risk areas since low-risk areas could have high resilience with proactive preparedness to allow sheltering in place. Fifth, the findings of the analysis in the context of Harris County in the 2017 Hurricane Harvey revealed disparities in the risk-resilience profile of lower median income communities which exhibited high risk and low resilience. The findings unveil that high-risk areas with higher income levels show a greater resilience status, while low-income areas exhibit low resilience status.

The study outcomes also set the stage for future studies to advance community resilience in two main directions. First, future studies can include additional features related to the coupled human-infrastructure systems performance when data is available. Second, the approach presented in this

study can be adopted for ex-post community resilience assessment across different events (in the same region) or across different regions to consistently compare the performance of coupled human-infrastructure systems across events and regions and their contributions to community resilience. Through these cross-regional and cross-events ex-post assessments, important features that positively contribute to resilience can be identified.

### **Data Availability**

The data that support the findings of this study are available from Ookla, Safegraph, INRIX, Microsoft Building Footprint, and Spectus, Inc, but restrictions apply to the availability of these data, which were used under license for the current study. The data can be accessed upon request. Other data we use in this study are all publicly available.

### **Code Availability**

The code that supports the findings of this study is available from the corresponding author upon request.

### **Acknowledgement**

The authors would like to acknowledge funding support from the NSF CAREER Faculty Early Career Development Program. The authors also would also like to acknowledge the data support from Ookla, Safegraph, INRIX, Microsoft Building Footprint, and Spectus, Inc. Any opinions, findings, conclusions, or recommendations expressed in this material are those of the authors and do not necessarily reflect the views of Ookla, Safegraph, INRIX, and Microsoft building footprint, and Spectus, Inc.

### **Reference**

- Beguería, S. (2006). Validation and Evaluation of Predictive Models in Hazard Assessment and Risk Management. *Natural Hazards*, 37(3), 315–329. <https://doi.org/10.1007/s11069-005-5182-6>
- Bhavathrathan, B. K., & Patil, G. R. (2015). Capacity uncertainty on urban road networks: A critical state and its applicability in resilience quantification. *Computers, Environment and Urban Systems*, 54, 108–118. <https://doi.org/10.1016/j.compenvurbsys.2015.07.005>
- Bronfman, N. C., Cisternas, P. C., Repetto, P. B., & Castañeda, J. V. (2019). Natural disaster preparedness in a multi-hazard environment: Characterizing the sociodemographic profile of those better (worse) prepared. *PloS one*, 14(4), e0214249.
- Brown, D., Saito, K., Spence, R., Chenvidyakarn, T., Adams, B., Mcmillan, A., Ltd, I., & Platt, S. (2008). *Indicators for Measuring, Monitoring and Evaluating Post-Disaster Recovery*.
- Bullock, J., Haddow, G., & Coppola, D. (2017). *Introduction to emergency management*. Butterworth-Heinemann.

- Chen, A. S., Hammond, M. J., Djordjević, S., Butler, D., Khan, D. M., & Veerbeek, W. (2016). From hazard to impact: Flood damage assessment tools for mega cities. *Natural Hazards*, 82(2), 857–890. <https://doi.org/10.1007/s11069-016-2223-2>
- Chen, Z., Gong, Z., Yang, S., Ma, Q., & Kan, C. (2020). Impact of extreme weather events on urban human flow: A perspective from location-based service data. *Computers, Environment and Urban Systems*, 83, 101520. <https://doi.org/10.1016/j.compenvurbsys.2020.101520>
- Coleman, N., Esmalian, A., & Mostafavi, A. (2020). Anatomy of susceptibility for shelter-in-place households facing infrastructure service disruptions caused by natural hazards. *International Journal of Disaster Risk Reduction*, 50, 101875. <https://doi.org/10.1016/j.ijdr.2020.101875>
- Cova, T. J., Drews, F. A., Siebeneck, L. K., & Musters, A. (2009). Protective Actions in Wildfires: Evacuate or Shelter-in-Place? *Natural Hazards Review*, 10(4), 151–162. [https://doi.org/10.1061/\(ASCE\)1527-6988\(2009\)10:4\(151\)](https://doi.org/10.1061/(ASCE)1527-6988(2009)10:4(151))
- Dargin, J. S., Li, Q., Jawer, G., Xiao, X., & Mostafavi, A. (2021). Compound hazards: An examination of how hurricane protective actions could increase transmission risk of COVID-19. *International Journal of Disaster Risk Reduction*, 65, 102560. <https://doi.org/10.1016/j.ijdr.2021.102560>
- Dong, S., Esmalian, A., Farahmand, H., & Mostafavi, A. (2020). An integrated physical-social analysis of disrupted access to critical facilities and community service-loss tolerance in urban flooding. *Computers, Environment and Urban Systems*, 80, 101443. <https://doi.org/10.1016/j.compenvurbsys.2019.101443>
- Dong, S., Malecha, M., Farahmand, H., Mostafavi, A., Berke, P. R., & Woodruff, S. C. (2021). Integrated infrastructure-plan analysis for resilience enhancement of post-hazards access to critical facilities. *Cities*, 117, 103318. <https://doi.org/10.1016/j.cities.2021.103318>
- Dong, S., Wang, H., Mostafavi, A., & Gao, J. (2019). Robust component: A robustness measure that incorporates access to critical facilities under disruptions. *Journal of The Royal Society Interface*, 16(157), 20190149. <https://doi.org/10.1098/rsif.2019.0149>
- Emanuel, K. (2017). Assessing the present and future probability of Hurricane Harvey's rainfall. *Proceedings of the National Academy of Sciences*, 114(48), 12681–12684. <https://doi.org/10.1073/pnas.1716222114>
- Fan, C., Jiang, X., & Mostafavi, A. (2020). A network percolation-based contagion model of flood propagation and recession in urban road networks. *Scientific Reports*, 10(1), 1–12.
- FEMA (Federal Emergency Management Agency). OpenFEMA Dataset: FIMA NFIP Redacted Claims - v1. 1–18 <https://www.fema.gov/openfema-data-page/fima-nfipredacted-claims-v1> (2023).
- Grinberger, A. Y., & Felsenstein, D. (2016). Dynamic agent based simulation of welfare effects of urban disasters. *Computers, Environment and Urban Systems*, 59, 129–141. <https://doi.org/10.1016/j.compenvurbsys.2016.06.005>
- Gupta, Y., Liu, Z., & Mostafavi, A. (2023). Digital Divide in Disasters: Investigating Spatial and Socioeconomic Disparities in Internet Service Disruptions During Extreme Weather Events [Preprint]. SSRN. <https://doi.org/10.2139/ssrn.4672649>

- Hubert, L. J., & Arabie, C. (1985). Evaluation of clustering algorithms using the silhouette score. *Journal of Classification*, 2(1), 195-213.
- Jain, A. K., & Dubes, R. C. (1988). Cluster validation techniques. *IEEE Transactions on Pattern Analysis and Machine Intelligence*, 10(2), 153-159.
- Jiang, Y., Yuan, F., Farahmand, H., Acharya, K., Zhang, J., & Mostafavi, A. (2022). Data-driven Tracking of the Bounce-back Path after Disasters: Critical Milestones of Population Activity Recovery and Their Spatial Inequality (arXiv:2211.11100). arXiv. <http://arxiv.org/abs/2211.11100>
- Kameshwar, S., Cox, D. T., Barbosa, A. R., Farokhnia, K., Park, H., Alam, M. S., & Van De Lindt, J. W. (2019). Probabilistic decision-support framework for community resilience: Incorporating multi-hazards, infrastructure interdependencies, and resilience goals in a Bayesian network. *Reliability Engineering & System Safety*, 191, 106568. <https://doi.org/10.1016/j.res.2019.106568>
- Kasmalkar, I. G., Serafin, K. A., Miao, Y., Bick, I. A., Ortolano, L., Ouyang, D., & Suckale, J. (2020). When floods hit the road: Resilience to flood-related traffic disruption in the San Francisco Bay Area and beyond. *Science Advances*, 6(32), eaba2423. <https://doi.org/10.1126/sciadv.aba2423>
- Kaufman, R., & Rousseeuw, P. J. (1990). Silhouettes: A graphical aid to the interpretation and validation of cluster analysis. *Journal of Computational and Applied Mathematics*, 20, 53-65.
- Kodinariya, T. M., & Makwana, P. R. (2013). Review on determining number of Cluster in K-means Clustering. *International Journal*, 1(6), 90-95.
- Lee CC, Chou C and Mostafavi A (2022) Specifying evacuation return and home-switch stability during shortterm disaster recovery using location-based data. *Scientific Reports* 12(1): 15987.
- Li, X., Jiang, Y., & Mostafavi, A. (2023). Hazard Exposure Heterophily in Socio-Spatial Networks Contributes to Post-Disaster Recovery in Low-Income Populations [Preprint]. SSRN. <https://doi.org/10.2139/ssrn.4645906>
- Lindell, M. K., Perry, R. W., Prater, C., & Nicholson, W. C. (2006). *Fundamentals of emergency management* (p. 485). Washington, DC: FEMA.
- Logan, T. M., Anderson, M. J., Williams, T. G., & Conrow, L. (2021). Measuring inequalities in urban systems: An approach for evaluating the distribution of amenities and burdens. *Computers, Environment and Urban Systems*, 86, 101590. <https://doi.org/10.1016/j.compenvurbsys.2020.101590>
- Meilă, P. (2005). Silhouette-based clustering validity revisited. *Journal of Machine Learning Research*, 6, 891-905.
- Microsoft/USBuildingFootprints. (2024). [Computer software]. Microsoft. <https://github.com/microsoft/USBuildingFootprints> (Original work published 2018)
- Mirbabaie, M., Bunker, D., Stieglitz, S., Marx, J., & Ehnis, C. (2020). Social media in times of crisis: Learning from Hurricane Harvey for the coronavirus disease 2019 pandemic response. *Journal of Information Technology*, 35(3), 195–213. <https://doi.org/10.1177/0268396220929258>



- Molinari, D., Menoni, S., Aronica, G. T., Ballio, F., Berni, N., Pandolfo, C., Stelluti, M., & Minucci, G. (2014). Ex post damage assessment: An Italian experience. *Natural Hazards and Earth System Sciences*, 14(4), 901–916. <https://doi.org/10.5194/nhess-14-901-2014>
- Pant, R., Thacker, S., Hall, J. W., Alderson, D., & Barr, S. (2018). Critical infrastructure impact assessment due to flood exposure. *Journal of Flood Risk Management*, 11(1), 22–33. <https://doi.org/10.1111/jfr3.12288>
- Podesta, C., Coleman, N., Esmalian, A., Yuan, F., & Mostafavi, A. (2021). Quantifying community resilience based on fluctuations in visits to points-of-interest derived from digital trace data. *Journal of The Royal Society Interface*, 18(177), 20210158. <https://doi.org/10.1098/rsif.2021.0158>
- Praharaj, S., Chen, T. D., Zahura, F. T., Behl, M., & Goodall, J. L. (2021). Estimating impacts of recurring flooding on roadway networks: A Norfolk, Virginia case study. *Natural Hazards*, 107(3), 2363–2387. <https://doi.org/10.1007/s11069-020-04427-5>
- Rajput, A. A., Nayak, S., Dong, S., & Mostafavi, A. (2022). Anatomy of Perturbed Traffic Networks during Urban Flooding (arXiv:2210.00403). arXiv. <http://arxiv.org/abs/2210.00403>
- Rosenheim, N., Guidotti, R., Gardoni, P., & Peacock, W. G. (2021). Integration of detailed household and housing unit characteristic data with critical infrastructure for post-hazard resilience modeling. *Sustainable and Resilient Infrastructure*, 6(6), 385–401. <https://doi.org/10.1080/23789689.2019.1681821>
- Vamvakeridou-Lyroudia, L. S., Chen, A. S., Khoury, M., Gibson, M. J., Kostaridis, A., Stewart, D., Wood, M., Djordjevic, S., & Savic, D. A. (2020). Assessing and visualising hazard impacts to enhance the resilience of Critical Infrastructures to urban flooding. *Science of The Total Environment*, 707, 136078. <https://doi.org/10.1016/j.scitotenv.2019.136078>
- Wang, Z., Lai, C., Chen, X., Yang, B., Zhao, S., & Bai, X. (2015). Flood hazard risk assessment model based on random forest. *Journal of Hydrology*, 527, 1130–1141. <https://doi.org/10.1016/j.jhydrol.2015.06.008>
- Williamson, D. F. (1989). The Box Plot: A Simple Visual Method to Interpret Data. *Annals of Internal Medicine*, 110(11), 916. <https://doi.org/10.7326/0003-4819-110-11-916>
- Yabe, T., Jones, N. K. W., Rao, P. S. C., Gonzalez, M. C., & Ukkusuri, S. V. (2022). Mobile phone location data for disasters: A review from natural hazards and epidemics. *Computers, Environment and Urban Systems*, 94, 101777. <https://doi.org/10.1016/j.compenvurbsys.2022.101777>
- Yuan, F., Fan, C., Farahmand, H., Coleman, N., Esmalian, A., Lee, C.-C., Patrascu, F. I., Zhang, C., Dong, S., & Mostafavi, A. (2022). Smart flood resilience: Harnessing community-scale big data for predictive flood risk monitoring, rapid impact assessment, and situational awareness. *Environmental Research: Infrastructure and Sustainability*, 2(2), 025006. <https://doi.org/10.1088/2634-4505/ac7251>
- Yuan, F., Xu, Y., Li, Q., & Mostafavi, A. (2022). Spatio-temporal graph convolutional networks for road network inundation status prediction during urban flooding. *Computers, Environment and Urban Systems*, 97, 101870. <https://doi.org/10.1016/j.compenvurbsys.2022.101870>

- Yuan, F., Yang, Y., Li, Q., & Mostafavi, A. (2021c). Unraveling the temporal importance of community-scale human activity features for rapid assessment of flood impacts. *IEEE Access*, 10, 1138–1150.
- Zhang, W., Gong, Z., Niu, C., Zhao, P., Ma, Q., & Zhao, P. (2022). Structural changes in intercity mobility networks of China during the COVID-19 outbreak: A weighted stochastic block modeling analysis. *Computers, Environment and Urban Systems*, 96, 101846. <https://doi.org/10.1016/j.compenvurbsys.2022.101846>